Numerical parametric study on ultimate load and ductility of concrete encased equal-leg angle steel composite columns

Zhang, Youyou; Liu, Yuqing; Xin, Haohui; He, Jun

Important note
To cite this publication, please use the final published version (if applicable).
Please check the document version above.

Numerical Parametric Study on Ultimate Load and Ductility of Concrete Encased Equal-leg Angle Steel Composite Columns

Youyou Zhang[a], Yuqing Liu[b], Haohui Xin[c*], Jun He[d]

[a]*Department of Civil and Environmental Engineering, University of California, Davis, CA, USA*

[b]*Department of Bridge Engineering, Tongji University, Shanghai, China*

[c]*Faculty of Civil Engineering and Geosciences, Delft University of Technology, Delft, the Netherlands*

[d]*School of Civil Engineering, Changsha University of Science & Technology, Changsha, PR China*

E-mail: H.Xin@tudelft.nl

Abstract

Steel-concrete composite high bridge pier has been applied increasingly in China and around the world. Most applied steel type in the composite piers are H-shaped steel and steel pipe, while seldom research or practice is associated with angle steel. This paper conducted parametric study on the composite column with equal-leg angle steel and aimed to investigate the ultimate load and displacement ductility of the composite columns with different parameters and shear connectors. The parameters include the type of shear connector (stud and perfobond connectors), the type of structural steel (H-shaped steel and angle steel), steel-plate hooping ratio, shear-span ratio, and axial compression ratio. Finite element analysis was conducted for each specimen, which incorporated the concrete confinement effect, as well as the inelastic behavior of concrete, structural steel, and longitudinal and transverse steel bars. The equal-leg angle steel composite column was found to have slightly higher strength and displacement ductility than H-shaped steel composite column. The increase of steel-plate hooping result in larger strength and displacement ductility for the composite column, and the increase of shear-span ratio and axial compression ratio decrease the displacement ductility. Research results suggest stud and perfobond shear connectors should be applied as axial compression ratio being larger than 0.2 and 0.3, respectively. This paper provides reference for research and engineering practice for the concrete-steel

composite columns and bridge piers.

1. Introduction

Reinforced concrete high bridge pier is widely applied in mountainous region. Extremely large quantities of reinforcing bars and highly concentrated hoop ties are required in the conventional high bridge pier to ensure sufficient strength, while the excessive reinforcing bars and hoop ties increases the construction difficulty and reduces the construction quality and efficiency. Hybrid Hollow High (3H) pier, provides an innovative solution to the excessive usage of steel bars in conventional bridge pier in which part of the axial direct reinforcing bars installed with the conventional method are replaced by the structural steel surrounded by spiral reinforcement, as shown in Figure 1. The 3H pier has several advantages comparing with traditional reinforced concrete pier: larger earthquake resistance, greater construction efficiency and economy, better construction quality and aesthetics, and environmental preservation [1].

In engineering practice and research, steel type in such steel-concrete composite bridge pier or column focuses on H-shaped steel or steel pipe, as shown in Figure 2. Michio et al. conducted experiment for eight 3H pier specimens which are half size of the actual bridge piers, and six pier specimens correspond to H-shaped steel and the other two correspond to steel pipe [2]. H-shaped steel composite high pier was applied in Sun Yat-Sen Freeway widening project to improve the construction quality and earthquake resistance[3]. El-Tawil and Deierlein investigated strength and ductility of nine concrete encased H-shaped steel composite columns using a fiber element model [4]. Soliman et al. experimentally studied ten encased steel concrete columns and concluded that concrete confinement affects the strength of the column, and steel pipe leads to better confinement than the H-shaped steel section [5]. Nonlinear 3-D finite element models were developed to analyses the strength and inelastic behavior of concrete encased H-shaped steel composite columns, which carefully

incorporated inelastic material properties as well as the concrete confinement effect [6, 7]. Shi et al. conducted static loading tests for concrete encased H-shaped steel composite columns and proposed formulas enable to evaluate the deformation capacity of columns with the consideration of axial load ratio, steel ratio, shear span ratio, fiber contents ratio and flange width [8].

Numerous researches on concrete encased composite columns are found to focus on H-shaped steel and steel pipe, whereas only a few research has been found to be associated with angle steel. Li conducted experiments for 23 high-strength concrete encased angle steel composite columns [9]. Zheng and Ji studied the seismic performance of nine angle-steel concrete column specimens [10]. Their researches of concrete angle steel composite columns are related to building structures, which have different design requirements with bridge piers, such as axial compression ratio and shear-span ratio, etc.

To obtain an in-depth understanding of high bridge pier with angle steel, we proposed the concrete encased equal-leg angle steel composite column in this study, which consists of concrete, angle steel and surrounded longitudinal and transvers reinforcement bars, as shown in Figure 3. Comparing with H-shaped steel or steel pipe, the equal-leg angle steel avoids complete separation of concrete inside and outside of the steel so that achieves the integrity of the column. Besides, the equal-leg angle steel composite column obtains larger moment of inertia of steel section credited to arranging angle-steel on the edges. Note in this paper, the research focuses on the single concrete encased steel composite column instead of the whole high bridge pier. The better understanding of a single column can provide reference to the further research and design for the whole high bridge pier.

The steel-plate hooping applied in the concrete encased equal-leg angle steel composite column provides multiple benefits: (1) good connection for four angle steel; (2) large confinement effect which increases the compressive strength for inner concrete; (3) short free length between steel-plate hooping along the column height which increases the column stability; (4) good shear connection between concrete and the structural steel. The steel-plate hooping and transverse reinforcement hooping provide confinement for the inner concrete as well as the middle concrete.

The main objective of this study is to numerically investigate the mechanical behavior of

concrete encased angel steel composite column with different parameters and shear connectors. Parametric study was conducted to investigate the effects of different steel type, steel-plate hooping ratio, shear-span ratio, and axial compression ratio on the strength and ductility of the composite columns. Detailed finite element models were developed which carefully considered the inelastic behavior of steel and concrete, longitudinal and transverse steel bars, as well as the concrete confinement effect. In addition, shear connection is important in concrete-steel composite structure. We proposed composite columns with different types of shear connectors and investigated the stress of angle steel and shear connectors under different axial compression ratio.
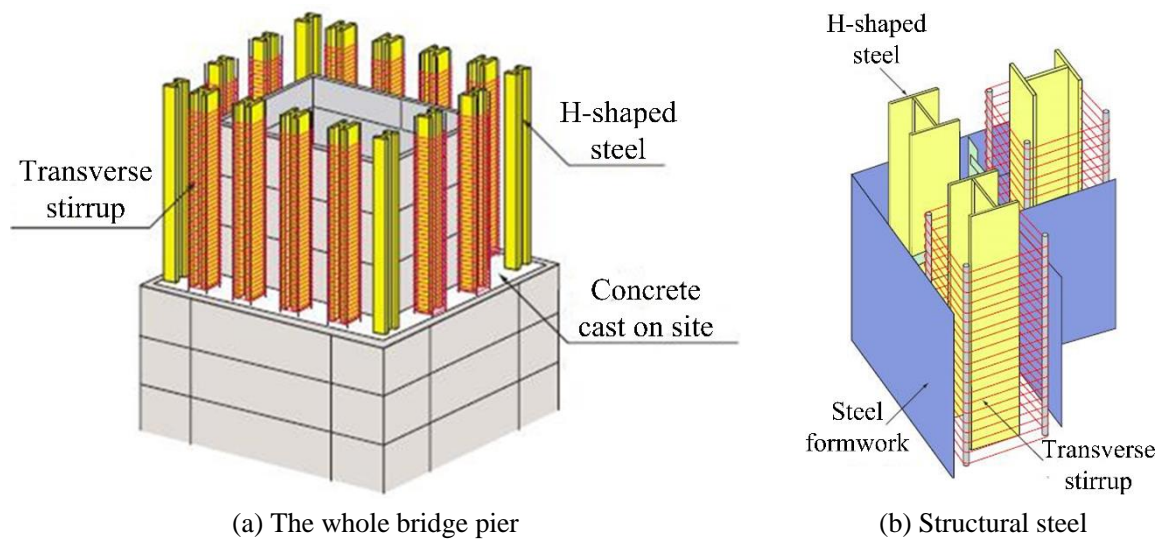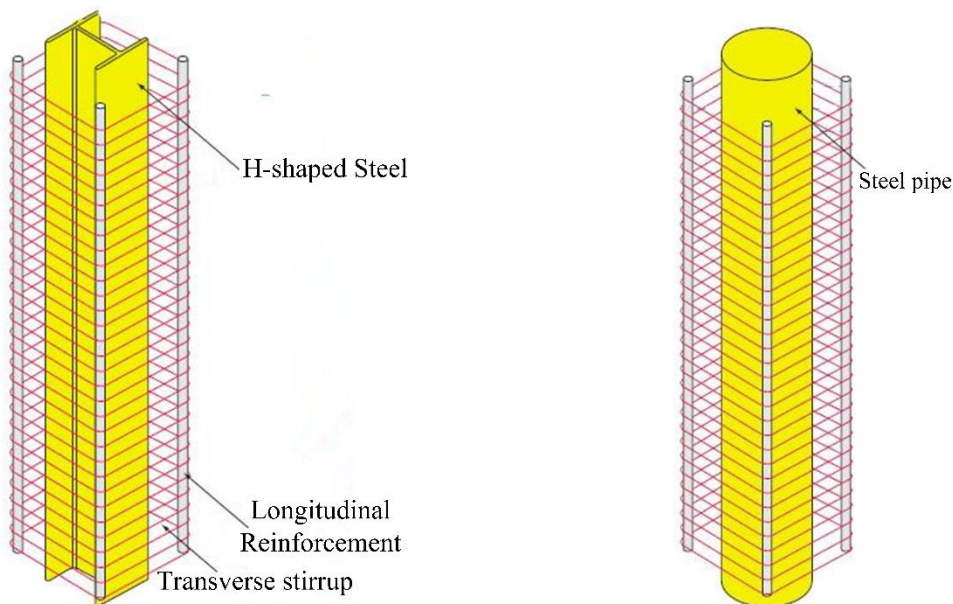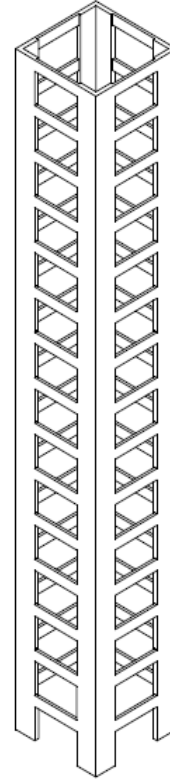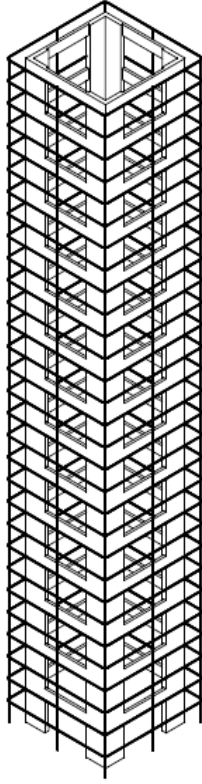

(a) The whole bridge pier   (b) Structural steel

Figure 1 Hybrid Hollow High (3H) pier

(a) Equal-leg angle steel surrounded by longitudinal
and transverse steel reinforcement

(b) Equal-leg angle steel

Figure 3 Equal-leg angle steel and reinforcing bars

2. Numerical Modeling

2.1 Parameters of Composite Columns

Four parameters are critical and carefully considered for the concrete encased steel composite column, which are sectional steel ratio, reinforcement ratio, shear-span ratio, and axial compression ratio [9].

(1) Sectional steel ratio

Sectional steel ratio in concrete encased steel composite column is the ratio of the cross-sectional area of the steel section to the total area of composite cross section.

Requirements for sectional steel ratio among different specifications and practices are not in agreement. AISC specification requires the sectional steel ratio shall be at least 1% [11]; Chinese codes for composite structure specify the sectional steel ratio should be in the range of 4%~15% [12]; researches suggest the sectional steel ratio to be 1.0%~8.0% [9,13]. In this paper, 4.44% is selected as the sectional steel ratio for all specimens.

(2) Shear-span ratio

Shear-span ratio is defined as the ratio of shear span to effective height of the column and this ratio affects the failure modes of the column. In reinforced concrete columns, shear-span ratio of less than 2 creates shear failure, larger than 4 creates flexural failure, and within the range of 2 to 4 corresponds to flexural-shear mode failure [12]. Flexural failure is a type of ductile failure, while shear failure and flexural-shear failure modes belong to brittle failure modes which should be avoided during design. Shear-span ratio also affects column strength. The bearing capacity of the column significantly decreases as the shear-span ratio increases. Thus, appropriate shear-span ratio should be designed aiming to get a favorable failure mode as well as enough strength.

Previous researches conducted experimental and analytical analysis for concrete encased steel composite columns with relatively small shear-span ratios for building structures: 1.0~2.5 [8], 2.0 [9], 3~5 [10], 2~3 [13], 2.0~2.5 [14], 3.25 [15], 3.0 [16]. In this paper, composite columns were studied for high piers instead of building structures, thus relatively large shear-span ratio of 3,5,8 and 10 was studied.

(3) Axial compression ratio

Axial compression ratio is defined as the ratio between the axial force and compressive strength of steel section and concrete, which is given by [17]:

$$n = \frac{N}{f_c A_c + f_s A_s} \tag{1}$$

Where N is the designed axial compressive force, f_c is the concrete axial compressive strength, A_c is the concrete compressive area, f_s is the compressive strength of steel section, and A_s is the area of steel section.

This study is originated from an engineering practice in Zhejiang province, China, in which the axial compression ratio for each single composite column is around 0.1. Thus, axial

compression ratio of 0.1 is regarded as a base parameter in this study, and parametric studies for axial compression ratio are conducted with the range of 0.1~0.5.
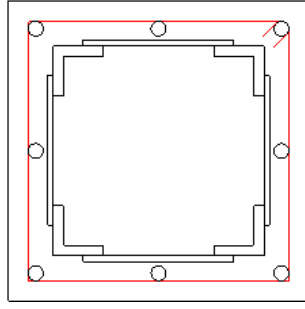
(4) Steel-plate volumetric ratio

Steel-plate volumetric ratio is defined as the ratio of the volume of steel-plate hooping to the volume of the core concrete enclosed by the steel-plate. The steel-plate ratio affects the ductility for the composite columns [9,16]. In this paper, volumetric of stirrup reinforcement ratio of steel plate is designed as 1.0%.

Parametric study was conducted in this study for the composite columns and the finite element models were developed for column specimens with varying parameters. Specimen SCP-A, as shown in Figure 4(a), is the base specimen to be used for comparison with other specimens. Equal-leg angle steel in SCP-A is 1.5m high, 50mm wide, and 5mm thick with the size of steel-plate hooping of 150mm, 25mm, and 6mm in length, height and thickness, respectively. The steel-plate hooping is arranged along the column height with the equal spacing of 100mm, which corresponds to the volumetric steel ratio being 1%. Eight longitudinal reinforcement bars are arranged outside the equal-leg angle steel with the diameter of 15 mm. Rectangular transverse reinforcement stirrups with 10-mm diameter are arranged along the column height with spacing of 50mm. The axial compressive force is set at 620kN, corresponding to the axial compression ratio of 0.1.

SCP-B in Figure 4(b) adopts the H-shaped steel with the same sectional steel ratio as in the SCP-A. Reinforcement stirrup is used for the H-shaped steel, which provides confinement for core concrete inside the H-shaped steel.

Table 1 lists parameters for different column specimens in this study. Specimens SCP-C1~C2 vary the steel-plate volumetric ratio from 1.0% in SCP-A to 1.2% and 1.4%, respectively. Specimens SCP-D1~D3 changes the shear-span ratio from 5 in SCP-A to 3, 8, 10, respectively. Specimens SCP-E1~E6 vary the axial compression ratio from 0.1 in SCP-A to 0.08, 0.15, 0.2, 0.3, 0.4, and 0.5, respectively.
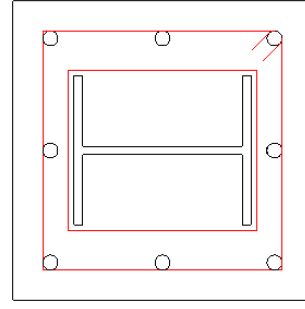
(a) SCP-A   (b) SCP-B

Figure 4 Cross section of specimens SRP-A and SRP-B

Table 1 Parameters of column specimens

Specimen	Section of steel	Shear steel plate volumetric ratio ρ_v/%	Longitudinal reinforcement	Transverse stirrup	Shear-span ratio λ	Axial compression ratio n
SCP-A	Angle Steel (∟50×50×10)	ρ_v = 0.8 % (25×150×6@100)	Ø15×8	Ø10@50	λ =5 (1.5 m)	n = 0.1 (620 kN)
SCP-B	H-Shaped Steel (H150×160×9×8)	ρ_v = 0.8 % (Ø10@50)	Ø15×8	Ø10@50	λ =5 (1.5 m)	n = 0.1 (620 kN)
SCP-C1	Angle Steel (∟50×50×10)	ρ_v = 1.2 % (25×150×6@83)	Ø15×8	Ø10@50	λ =5 (1.5 m)	n = 0.1 (620 kN)
SCP-C2	Angle Steel (∟50×50×10)	ρ_v = 1.4 % (25×150×6@70)	Ø15×8	Ø10@50	λ =5 (1.5 m)	n = 0.1 (620 kN)
SCP-D1	Angle Steel (∟50×50×10)	ρ_v = 0.8 % (25×150×6@100)	Ø15×8	Ø10@50	λ = 3 (0.9 m)	n = 0.1 (620 kN)
SCP-D2	Angle Steel (∟50×50×10)	ρ_v = 0.8 % (25×150×6@100)	Ø15×8	Ø10@50	λ = 8 (2.4 m)	n = 0.1 (620 kN)
SCP-D3	Angle Steel (∟50×50×10)	ρ_v = 0.8 % (25×150×6@100)	Ø15×8	Ø10@50	λ = 10 (3m)	n = 0.1 (620 kN)
SCP-E1	Angle Steel (∟50×50×10)	ρ_v = 0.8 % (25×150×6@100)	Ø15×8	Ø10@50	λ =5 (1.5m)	n = 0.08 (496 kN)
SCP-E2	Angle Steel (∟50×50×10)	ρ_v = 0.8 % (25×150×6@100)	Ø15×8	Ø10@50	λ =5 (1.5m)	n = 0.15 (930 kN)
SCP-E3	Angle Steel (∟50×50×10)	ρ_v = 0.8 % (25×150×6@100)	Ø15×8	Ø10@50	λ =5 (1.5m)	n = 0.2 (1240 kN)
SCP-E4	Angle Steel (∟50×50×10)	ρ_v = 0.8 % (25×150×6@100)	Ø15×8	Ø10@50	λ =5 (1.5m)	n = 0.3 (1860 kN)
SCP-E5	Angle Steel (∟50×50×10)	ρ_v = 0.8 % (25×150×6@100)	Ø15×8	Ø10@50	λ =5 (1.5m)	n = 0.4 (2480 kN)
SCP-E6	Angle Steel (∟50×50×10)	ρ_v = 0.8 % (25×150×6@100)	Ø15×8	Ø10@50	λ =5 (1.5m)	n = 0.5 (3100 kN)

2.2 Modeling Approach

The proposed concrete encased equal-leg angel steel composite columns consist of four components: concrete, steel section, longitudinal and transverse reinforcement bars, as shown in Figure 5. Earlier researches on concrete encased columns have shown that steel section and reinforcement stirrups would provide different levels of concrete confinement, dividing the composite columns into three main zones [4, 6, 7], as shown in Figure 6: (1) unconfined concrete zone consists of the concrete cover and the parabolic arching between the reinforcement bars. Note that the parabola was assumed to have an initial tangent slope of 45 degree; (2) highly confined zone inside the perimeter of the structural steel and the arching formed by the steel section; and (3) partially confined concrete zone which refers to concrete section between unconfined and highly confined concrete zones. The confinement depends on factors including material properties of concrete, steel section and reinforcement bars, the steel section geometry, diameter, spacing, layout and number of the longitudinal and transverse reinforcement bars, etc.

In the FE modeling, the parabolic concrete zones are adjusted into rectangular zones for modelling simplification, as shown in Figures 7 and 8. For the encased H-shaped steel composite column, the highly confined concrete is taken from the web of the steel section to the vertex of parabola between the two flanges; the partially confined concrete is taken from the vertex of parabola between longitudinal reinforcement bars to the vertex of parabola between flanges; and the unconfined concrete is the remaining external zone. Similar simplified method was applied for the encased equal-leg angle steel composite column: the highly confined concrete zone is the square area passing through four vertexes formed between angle legs; the partially confined concrete is taken from the vertexes of the parabola between longitudinal reinforcement bars to the vertex of parabola between angle legs; and the unconfined concrete is the remaining external zone.

(a) The whole column   (b) Equal-leg angle steel   (c) Longitudinal and transverse reinforcement bars
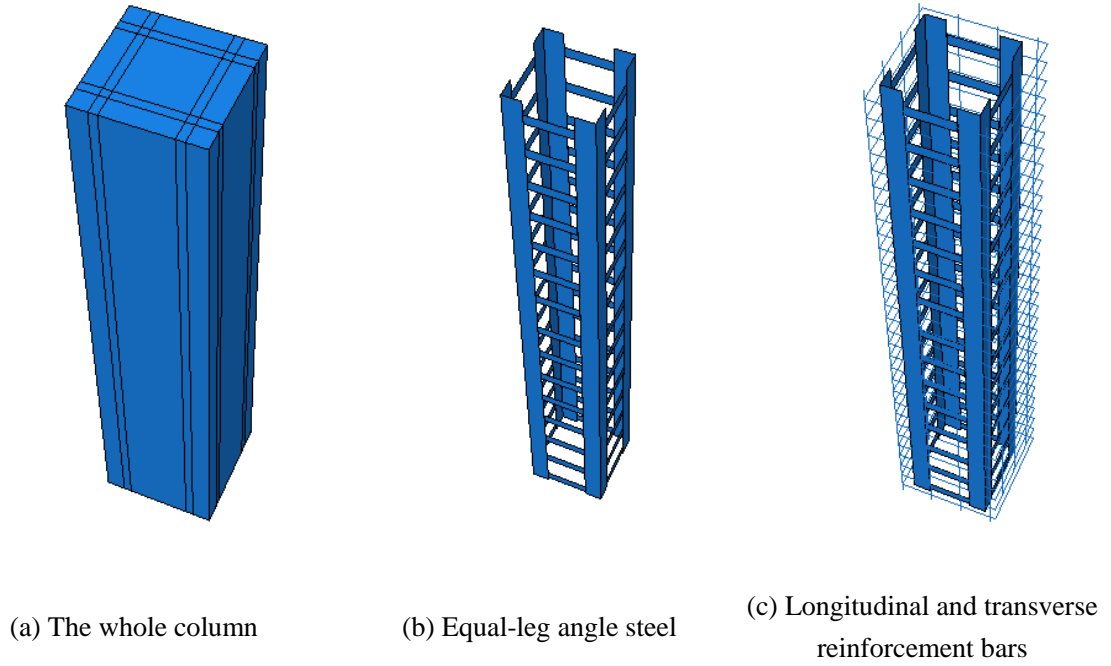
Figure 5 Finite element modelling for the concrete encased equal-leg angle steel composite column

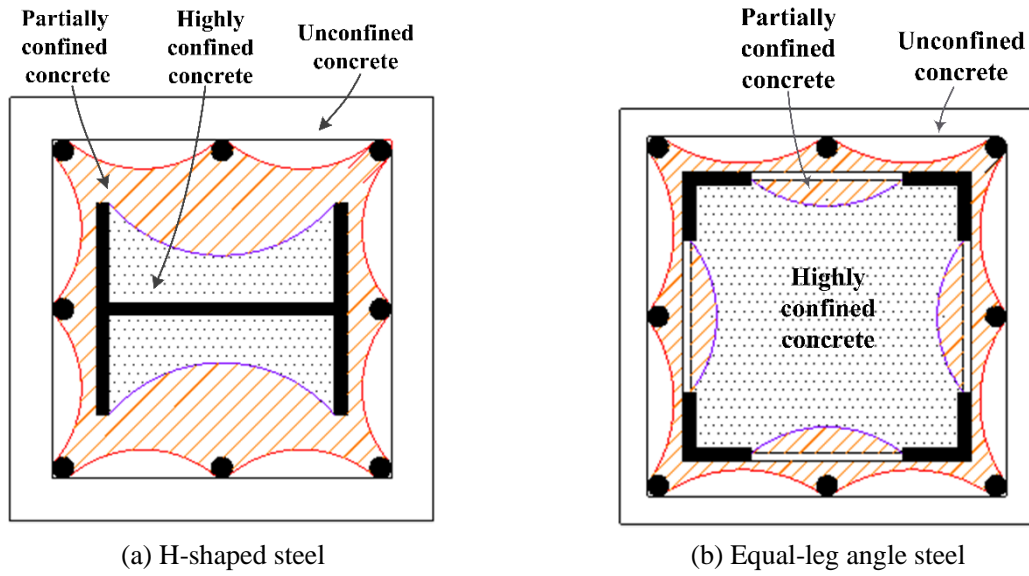(a) H-shaped steel   (b) Equal-leg angle steel

Figure 6 Confinement zones in concrete encased steel composite columns

(a) Original confinement zones of SCP-B   (b) Simplified confinement zones of SCP-B
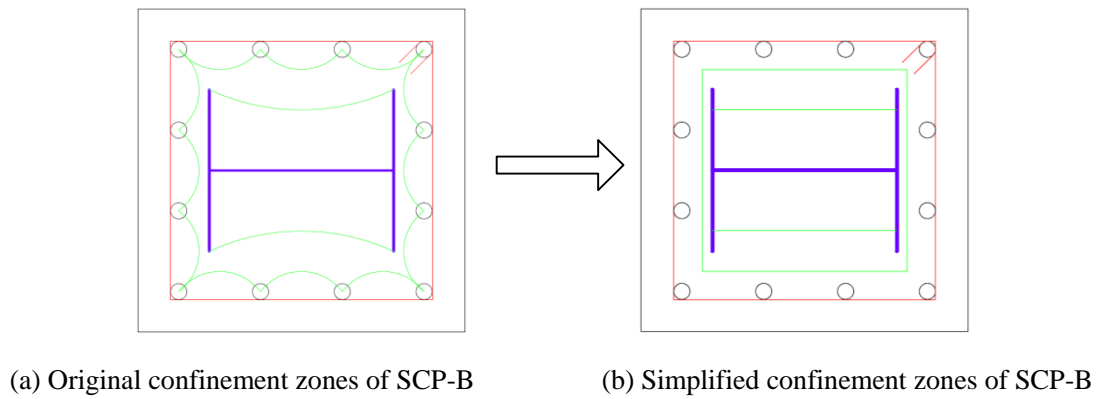
Figure 7 Confinement zones of SCP-B
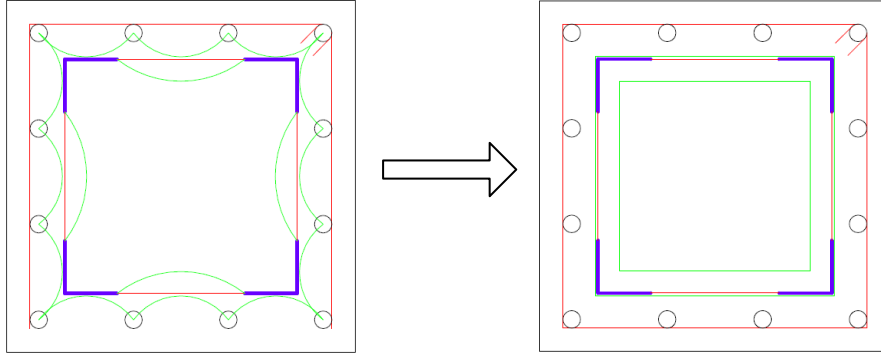
(a) Original confinement zones for SCP-A   (b) Simplified confinement zones for SCP-A

Figure 8 Confinement zones for SCP-A

2.3 Constitutive Model for Concrete

Mander's model is a unified stress-strain model which has been widely adopted for confined concrete modelling [18]. In this study, the Mander's model was selected for modelling the highly confined, partially confined and unconfined concrete, as shown in Figure 9. The longitudinal compressive stress-strain curve for confined concrete is given by

$$f_c = \frac{f'_{cc} x r}{r - 1 + x^r} \tag{2}$$

with

$$x = \frac{\varepsilon_c}{\varepsilon'_{cc}} \tag{3}$$

$$r = \frac{E_c}{E_c - E_{sec}} \tag{4}$$

where f'_{cc} is compressive strength (peak stress) of confined concrete; ε'_{cc} is the strain at compressive strength; E_c is the tangent elastic modulus of the concrete; and E_{sec} is the secant modulus of confined concrete at peak stress.

The compressive strength of confined concrete f'_{cc} is determined by the compressive strength of unconfined concrete f'_c and the effective lateral confining stress f'_l. The compressive strength of confined concrete f'_{cc} is expressed by

$$f'_{cc} = f'_c \left[\left(2.254 \sqrt{1 + \frac{7.94 f'_l}{f'_c}} - 2 \frac{f'_l}{f'_c} \right) - 1.254 \right] \tag{5}$$

The effective lateral confining stress f'_l is related to the volumetric ratio and yield strength of lateral reinforcement and the area of effectively confined concrete core.

The strain at maximum confined concrete stress ε'_{cc} is given by

$$\varepsilon'_{cc} = \varepsilon'_{c0}[1 + 5(\frac{f'_{cc}}{f'_c} - 1)] \tag{6}$$

where f'_c is the compressive strength of unconfined concrete and ε'_{c0} is the strain at maximum unconfined concrete stress.

The secant modulus of confined concrete at maximum confined stress is dependent on the compressive strength of confined concrete f'_{cc} and the strain at maximum confined concrete stress ε'_{cc}, that is:

$$E_{sec} = \frac{f'_{cc}}{\varepsilon'_{cc}} \tag{7}$$

The structural steel is taken into account in concrete encased steel composite columns to determine the confining stress, and a higher compressive strength f'_{cc} is obtained for the highly confined concrete region. The stress-strain curve for unconfined concrete is also determined by Eq.(2), just substituting $f'_l = 0$ in Eq.(5) and $\varepsilon'_{c0} = 0.002$ in Eq.(6).
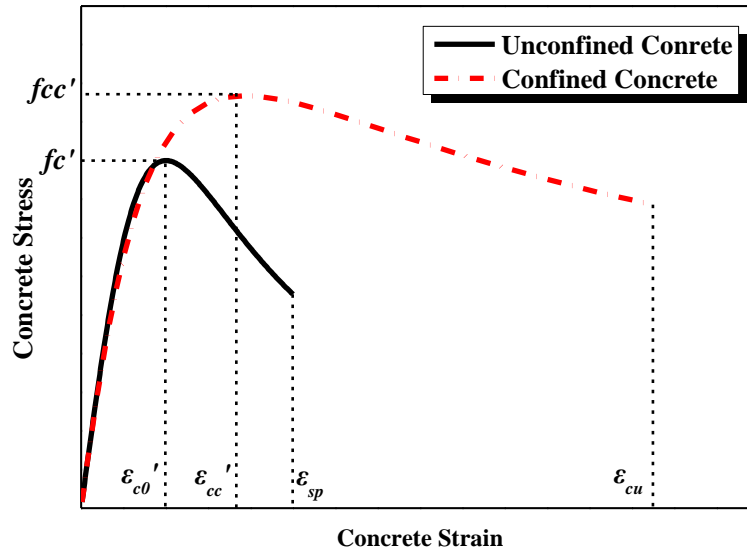
Figure 9 Stress-strain curves for unconfined and confined concrete

2.4 Constitutive Model for Structural Steel Section and Reinforcement Bars

Figures 10(a) and (b) show the simplified stress-strain curves for the steel section and reinforcing steel bars in tension, respectively. They both use the three-fold line constitutive

models, values of which were obtained from the material laboratory tests [19]. σ_{ys} and ε_{ys} represent yield stress and yield strain for the structural steel, respectively, and σ_{yr} and ε_{yr} represent yield stress and yield strain for reinforcement bars, respectively. It is assumed that the stress-strain behavior is identical in compression for both the structural steel and reinforcing steel. In this study, it is assumed that the structural steel has the yield stress of 345 MPa, and the reinforcing bars has the yield stress of 335 MPa. The longitudinal steel bar has the diameter of 15 mm, and the transverse steel hooping has the diameter of 10 mm.
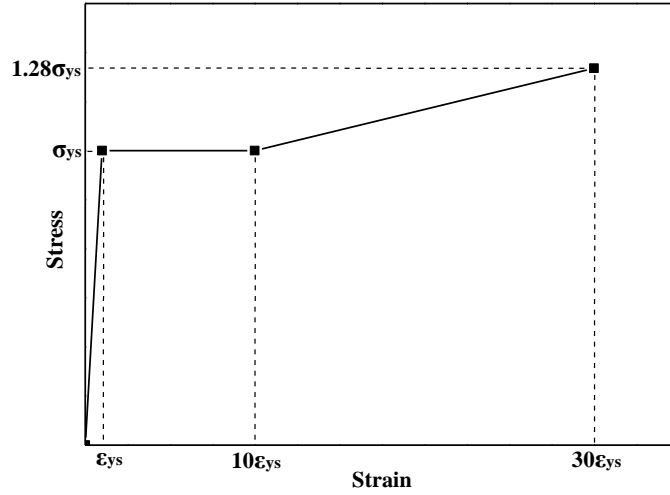
(a) Structural steel
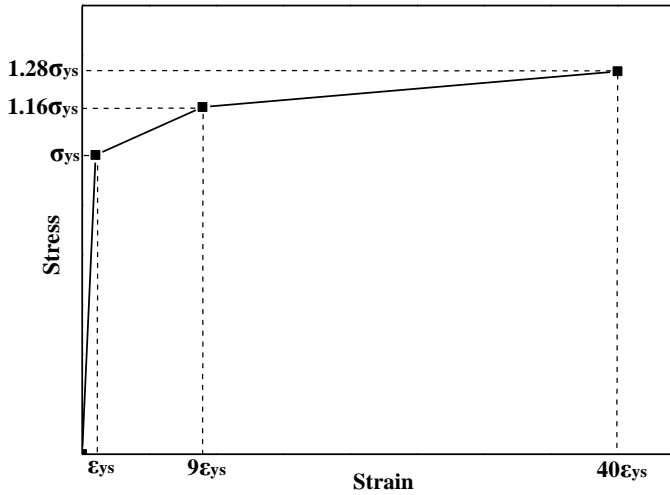
(b) Reinforced steel bar

Figure 10 Stress-strain relation for structural steel and reinforcing steel

2.5 Finite Element Model

In this study, finite element analysis platform ABAQUS [20] was selected for the

simulation of the concrete encased steel composite columns. Different types of elements were specified for different parts of the columns with the consideration of modelling accuracy and efficiency. In addition, different mesh sizes for each component were tried to select the reasonable mesh which provides both reliable results and less computational time. Concrete was modeled by the solid element C3D8R with three degrees of freedom and the mesh size is set as 1(length): 1(width): 2(depth). Structural steel was modeled by shell element S4R with six degrees of freedom and the mesh size is set as 1(length):1(width). Longitudinal and transverse reinforcement bars were modelled by using truss element T3D2. It is worth mentioning that for the solid element C3D8R, mesh sizes vary in different regions, namely, the inner concrete adopts finer mesh than the outer concrete as the inner concrete contact with the structural steel so that necessitate the more-refined analysis.

The structural-concrete, the longitudinal and transverse reinforcement bar-concrete interfaces were modelled by embedded constraint techniques [20], as shown in Figure 11. Nodes of steel section and reinforcement bars were set as embedded nodes, and nodes of concrete are set as hosted nodes. The composite columns are fixed at the bottom and free at the top, as shown in Figure 12. In the engineering practice, dead loads of superstructure account for a much larger percentage of axial force than live loads, meaning the axial compression force vary with a small magnitude and can be treated as a constant in finite element modelling; whereas horizontal loads for bridge columns vary due to several factors such as temperature change, horizontal vehicle braking force, etc. Considering the load application in the finite element modeling should be consistent with practice, the loads are applied by two steps: first, a constant axial force is applied at the column top; then, gradually increasing horizontal load is added at the column top until the column failure.
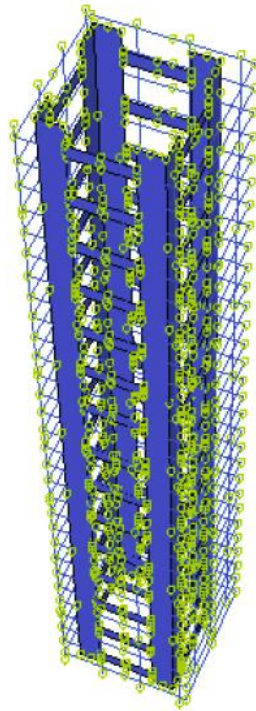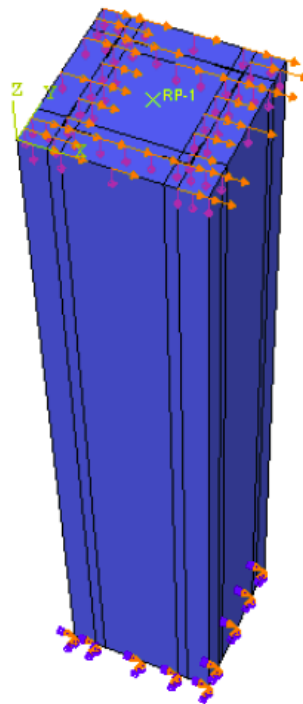
Figure 11 Contact modelling

Figure 12 Boundary condition and load application

3. Parametric Study Results

3.1 Type of Steel Section

Figure 13 shows lateral load-displacement curves for specimens SCP-A and SCP-B. Important characteristic are obtained from the curves, including yield displacement, maximum displacement, maximum load, initial secant stiffness, and displacement ductility. Displacement ductility is used to reflect the ability of the composite column to undergo large deformation in the inelastic range without a significant reduction in strength. The displacement ductility μ of the composite column is defined as

$$\mu = \Delta_u / \Delta_y \tag{8}$$

where Δ_u is the maximum displacement, and Δ_y is the yield displacement, which refers to the yield displacement of the equivalent elastic-plastic system with reduced stiffness found as the secant stiffness at 75% of the maximum lateral load H_u of the real system, as shown in Figure 14 [21].

Table 2 tabulates mechanical characteristics of specimen SCP-A and SCP-B, and Figure 15 shows displacement ductility of these two specimens. Maximum load and initial secant stiffness of specimen SCP-A are 7.71% and 10.04% higher than corresponding characteristics of SCP-B. Displacement ductility of SCP-A and SCP-B are 2.37 and 2.27, respectively, with the ductility of SCP-A being 4.41% higher than SCP-B. Slightly larger strength, stiffness, and displacement ductility of SCP-A indicates that equal-leg angle steel section encased in concrete column is mechanically superior than H-shaped steel with the same sectional steel ratio, steel-plate hooping ratio, axial compressive ratio, and shear-span ratio.

16
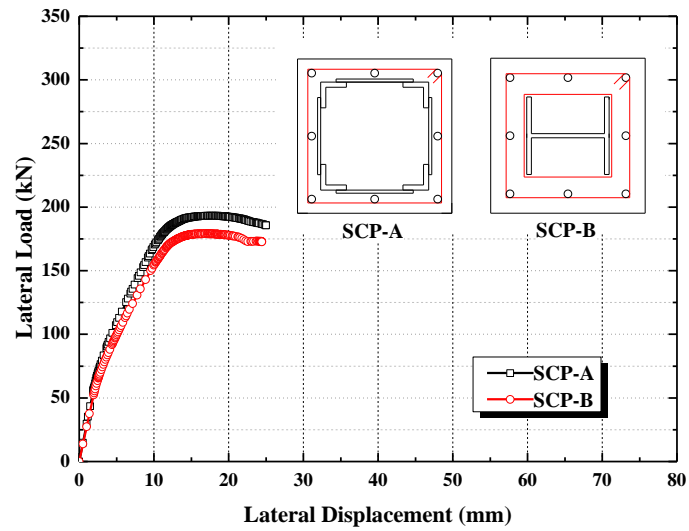
Figure 13 Lateral load-displacement curves of specimen SCP-A and SCP-B
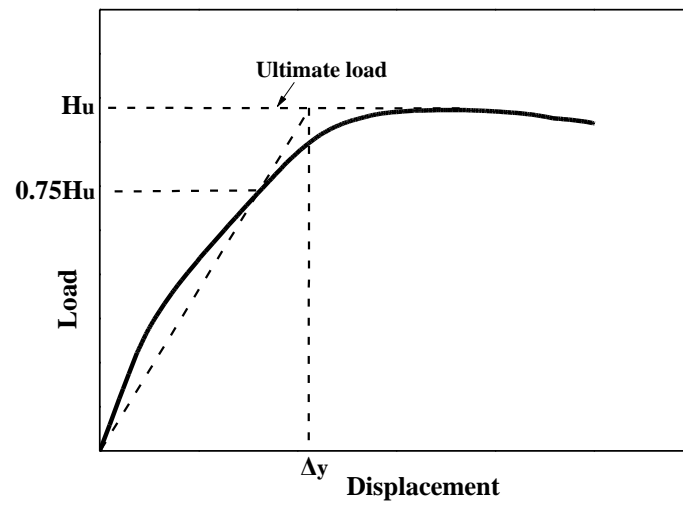
Figure 14 Definition of displacement ductility ratio

Table 2 Physics characteristics of specimens SCP-A and SCP-B

Specimen	Yield displacement (mm)	Maximum displacement (mm)	Maximum load (KN)	Initial secant stiffness (kN/mm)	Displacement ductility
SCP-A	10.54	25.02	192.85	18.30	2.37
SCP-B	10.77	24.46	179.05	16.63	2.27

17
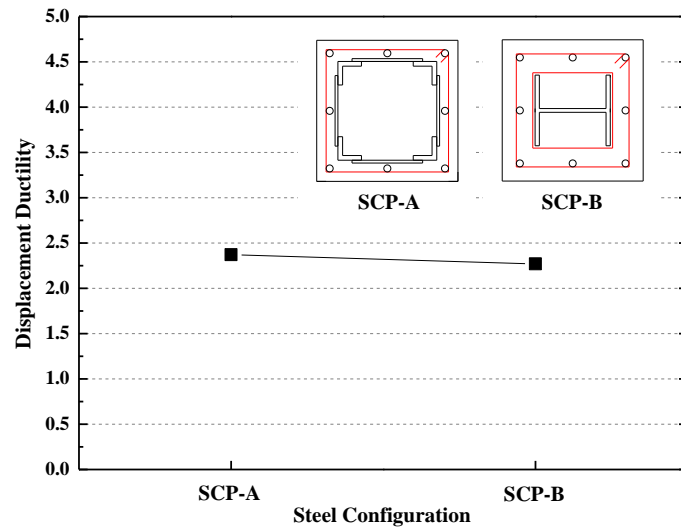
Figure 15 Displacement ductility of specimen SCP-A and SCP-B

3.2 Steel-Plate Hooping Ratio

Figure 16 shows the lateral load-displacement curves for specimens SCP-A, SCP-C1 and SCP-C2, with varying steel-plate hooping ratio of 1.0%, 1.2%, and 1.4%, respectively. Initial stiffness of the composite column rises as the steel-plate hooping ratio increases. Displacement ductility of the three specimens are listed in Table 3 and plotted in Figure 17, with values of 2.37, 3.14, 4.39 for Specimen SCP-A, SCP-C1, and SCP-C2, respectively. Concrete strain continually increases during the loading process, making the core concrete expand outward. The mutual effect between expanded concrete and steel-plate hooping provides the confinement to concrete. The larger steel-plate hooping ratio, the more significant confinement to concrete would be achieved. This confinement improves the ductility of concrete material, and further increase the displacement ductility of the composite column.
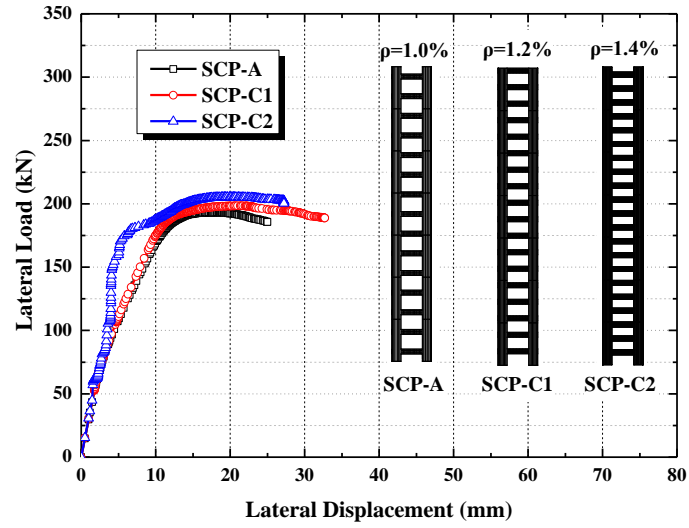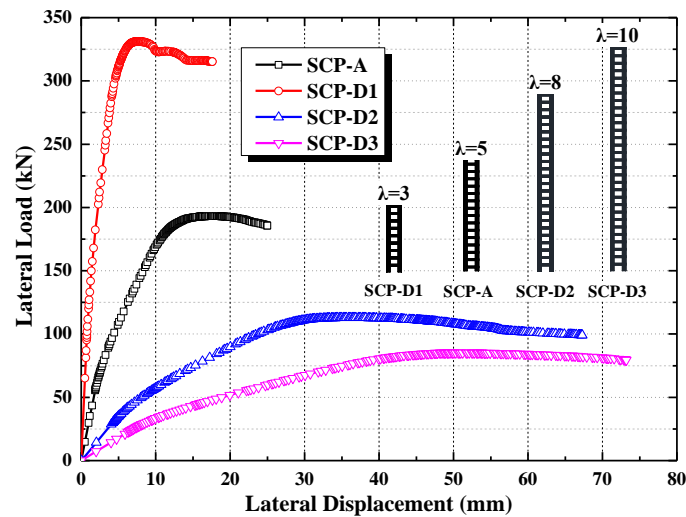
Figure 16 Lateral load-displacement curves of specimens with different steel-plate hooping ratio

Table 3 Physics characteristics of specimens with different steel-plate hooping ratio

Specimen	Yield displacement (mm)	Maximum displacement (mm)	Maximum load (KN)	Initial secant stiffness (kN/mm)	Displacement ductility
SCP-A	10.54	25.02	192.85	18.30	2.37
SCP-C1	10.42	32.70	198.30	19.02	3.14
SCP-C2	6.20	27.22	205.23	33.11	4.39
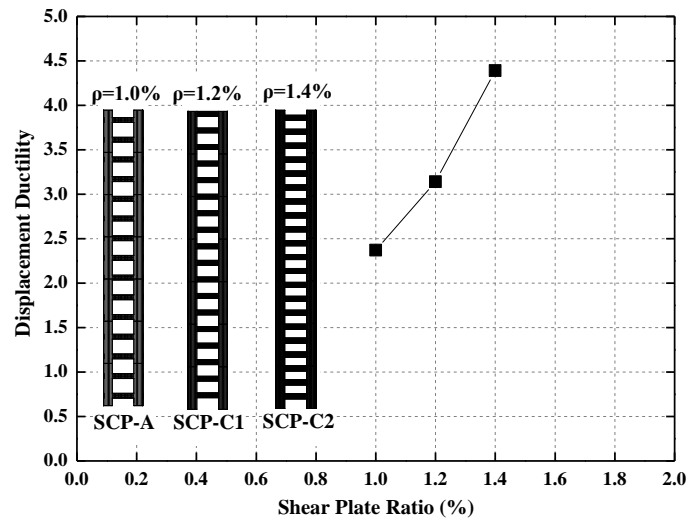
Figure 17 Displacement ductility for specimens with different steel-plate hooping ratio

3.3 Shear-span Ratio

Figure 18 shows the lateral load-displacement curves for specimen SCP-A, SCP-D1, SCP-D2, and SCP-D3, with varying shear-span ratio of 5, 3, 8 and 10, respectively. The maximum lateral load of these four specimens vary significantly with 330.97 kN, 192.85 kN, 112.90 kN, and 85.19 kN for SCP-A, SCP-D1, SCP-D2, and SCP-D3, respectively, showing that shear-span ratio greatly affects column strength. As listed in Table 4, displacement ductility of SCP-D1, SCP-A, SCP-D2, and SCP-D3 are 4.10, 2.37, 2.75, 1.98, respectively, which shows a general decreasing trend with the rising shear-span ratio (Figure 19). This finding is inconsistent with previous researches, which show displacement ductility of concrete encased steel composite columns reduce as shear-span ratio increases [9,10,16]. This inconsistence could result from different shear-span ratios: the shear-span ratio in previous researches ranges from 1-3, whereas in this study ranges from 3-10. In this study, although maximum displacement increases significantly as the shear-span ratio increase, the yield displacement rises with a greater speed, making the displacement ductility shows a decreasing trend.

Figure 18 Lateral load-displacement curves of specimen with different shear-span ratio

Table 4 Physics characteristics of specimens with different shear-span ratio

Specimen	Yield displacement (mm)	Maximum displacement (mm)	Maximum load (KN)	Initial secant stiffness (kN/mm)	Displacement ductility
SCP-D1	4.30	17.62	330.97	76.92	4.10
SCP-A	10.54	25.02	192.85	18.30	2.37
SCP-D2	24.50	67.30	112.90	4.61	2.75
SCP-D3	36.97	73.22	85.19	2.30	1.98
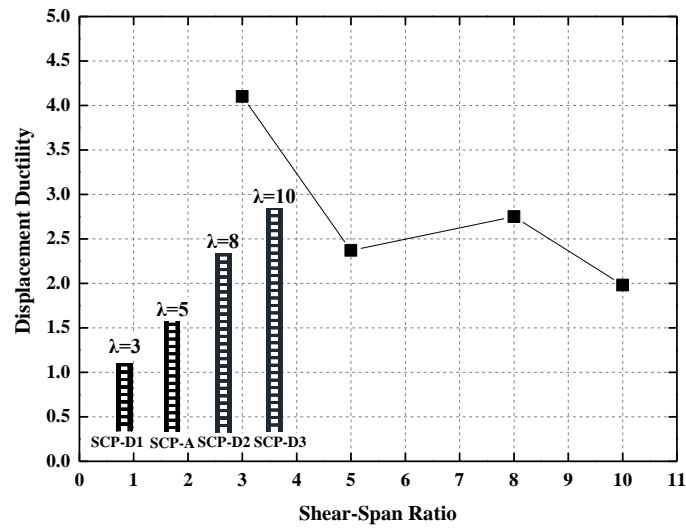
Figure 19 Displacement ductility for specimens with different shear-span ratio

3.4 Axial Compression Ratio

Figure 20 shows the lateral load-displacement curves for specimens SCP-A, and SCP E1~E6, with varying axial compression ratios ranging from 0.08~0.5. As axial compression ratio increases, initial secant stiffness increases, and the maximum displacement decreases (Table 5). Displacement ductility almost linearly vary from 2.52 for SCP-E1 decreasing to 0.43 for SCP-E6, with the drop rate of 82.9%, as shown in Figure 21. With increasing axial ratio, concrete strain and stress before applying the lateral load is getting larger. Thus, the ultimate deformation capability of concrete material decreases, causing the reduction of displacement ratio. Besides, larger axial compression creates greater second moment(p-Δ effect), making the composite column being more likely to reach the strength and thus decreasing the ultimate displacement and displacement ductility.

Table 5 Physics characteristics of specimens with different axial compression ratio

Specimen	Yield displacement (mm)	Maximum displacement (mm)	Maximum load (KN)	Initial secant stiffness (kN/mm)	Displacement ductility
SCP-E1	10.63	26.80	188.03	17.69	2.52
SCP-A	10.54	25.02	192.85	18.30	2.37
SCP-E2	10.47	22.02	205.30	19.60	2.10
SCP-E3	10.41	20.58	214.31	21.51	1.68
SCP-E4	10.01	20.38	221.51	23.42	1.26
SCP-E5	9.09	17.97	211.45	25.32	0.84
SCP-E6	8.15	16.80	188.19	27.23	0.43
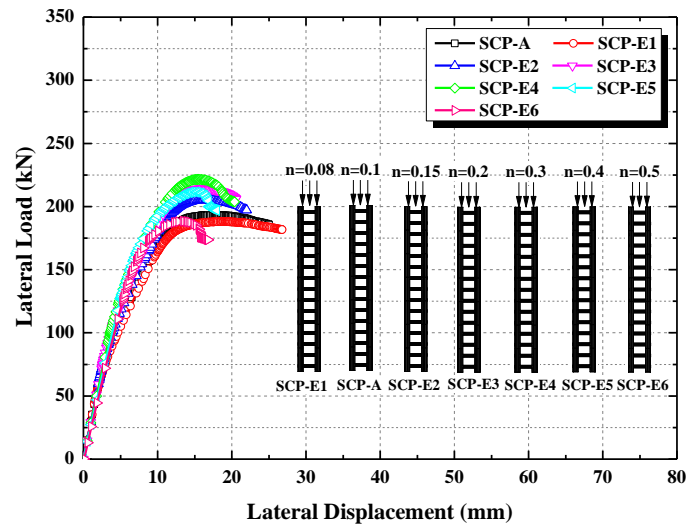
Figure 20 Lateral load-displacement curves of specimens with different axial compression ratio
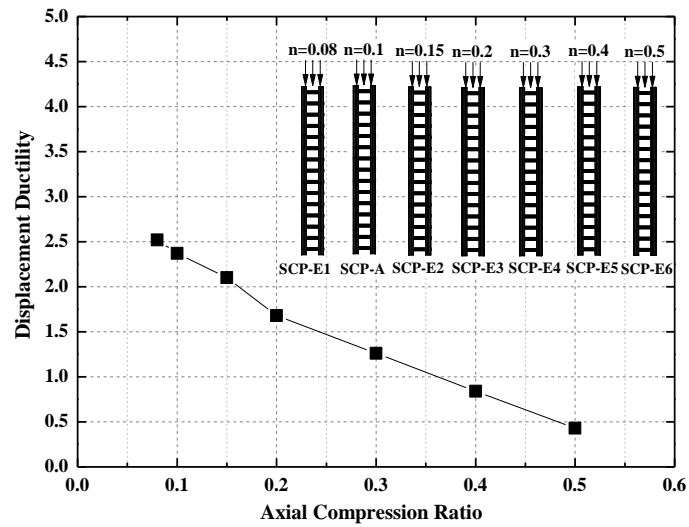
Figure 21 Displacement ductility of specimens with different axial compression ratio

Figure 22 shows the $N_u - M_u$ curve for composite columns under different axial compression ratios, where N_u is the maximum axial compression and M_u is the is the maximum bending moment at the bottom section. Compression ratio of 0.35 corresponds to the balance failure mode. Compression failure occurs when axial compression ratio is smaller than 0.35, and tension failure occurs when the ratio is larger than 0.35.

Figures 23(a)–(e) show normal stress cloud image at column bottom under axial compression ratio of 0.1,0.2,0.3,0.4, and 0.5, respectively. Note that concrete in red areas is in tension, and the left edge of red area in these plots can be regarded as the location of neutral axis. Figure 24 shows the relative compression zone height of cross-section at column bottom. As the axial compression ratio increases from 0.1 to 0.5, the area of concrete in tension reduces (Figure 23) and the relative compression zone height rises (Figure 24), indicating axial compression would significantly affect section strain distribution during loading and at failure.
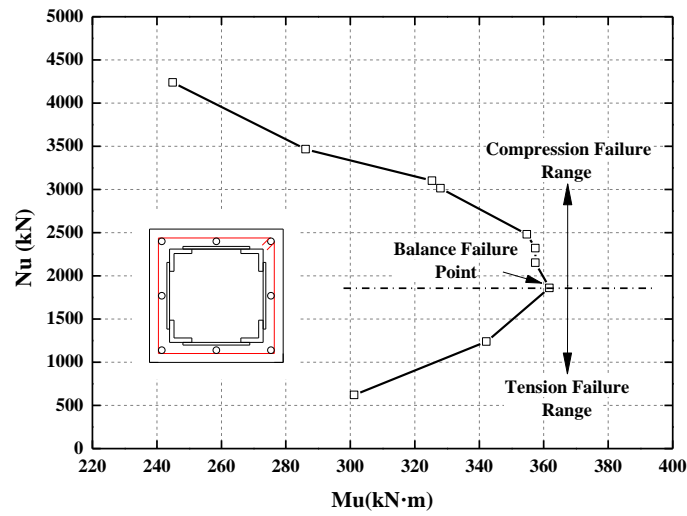
Figure 22 $N_u - M_u$ curve of composite columns under different axial compression ratio

(a) n=0.1

(b) n=0.2

(c) n=0.3

(d) n=0.4

(e) n=0.5
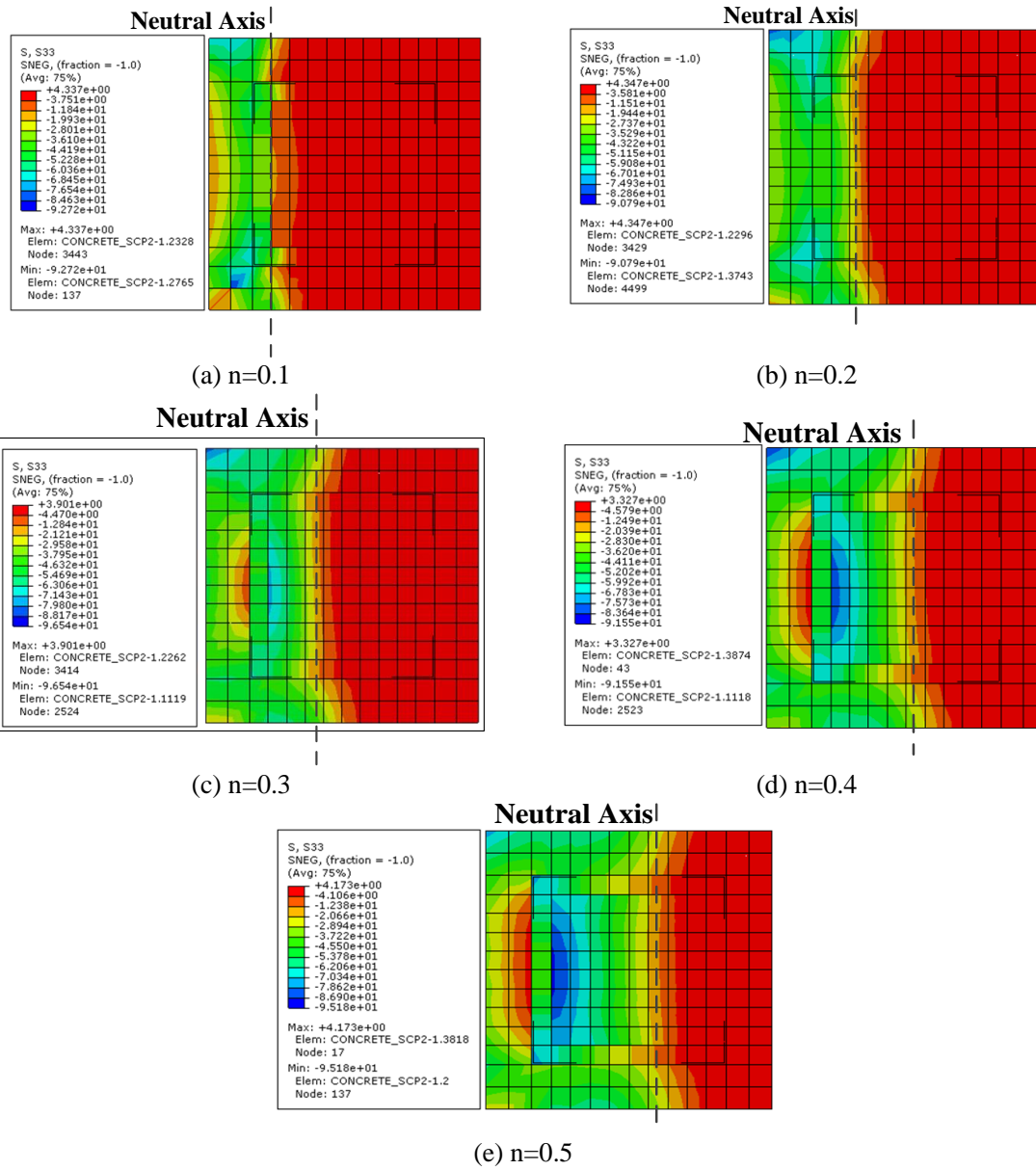
Figure 23 Normal stress cloud image of cross-section at column bottom with different axial compression ratio
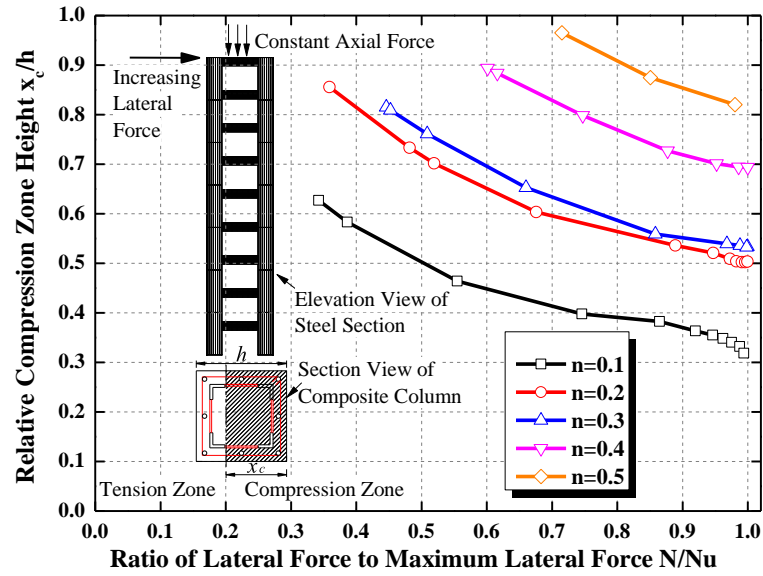
Figure 24 Relative compression zone height of section at column bottom

Figures 25(a)-(d) show concrete strain distribution along cross-section under different axial compression ratios. Different curves in the same plot related to different relative lateral forces, which are the ratios between the lateral force during the loading process to the maximum lateral force at failure. When the axial compression ratio is 0.1(Figure 25(a)), the concrete strain at various depth of the cross section presents a linear distribution. The distance between neutral axis and the compression fiber is relatively small, about one third of the total depth of the cross-section. Maximum strain at tension fiber is much larger than that at compression fiber, indicating a typical tension failure mode of the composite column. As the axial compression ratio increases, the distance between neutral axis and the compression fiber is continually increasing (Figures 25(b)~(d)). Besides, the maximum strain at compression fiber increases, whereas at tension fiber decrease. When the axial compression ratio reaches to 0.5 (Figure 25(d)), structural steel in compression side fails while in tension side keeps small strain, showing a typical compression failure mode. Moreover, strain distribution in compression zone no longer satisfy the linearly distribution when the axial compression zone is relatively large, as shown in Figures 25(b)-(d).

(a) n=0.1   (b) n=0.2

(c) n=0.4   (d) n=0.5
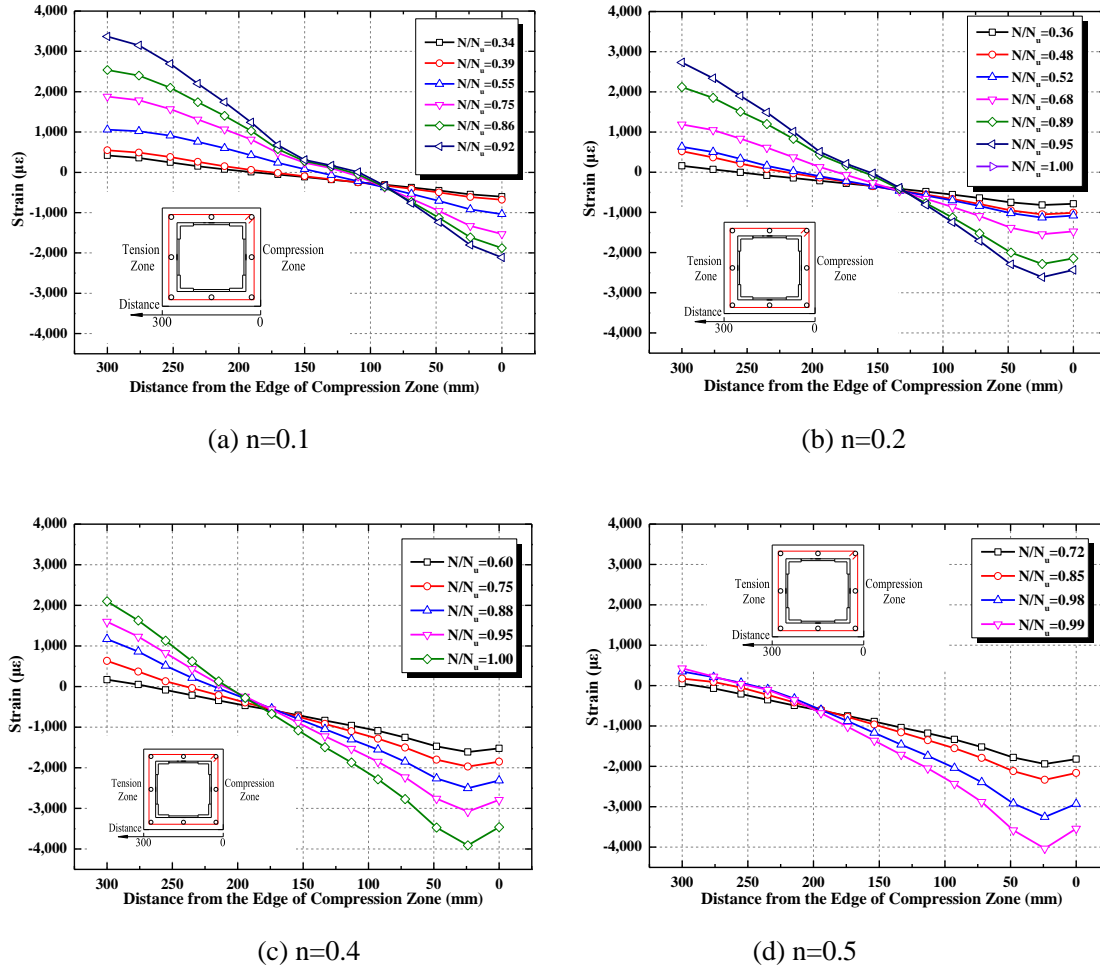
Figure 25 Concrete strain distribution along cross-section with different axial compression ratio

4. Shear Connectors Effects

4.1 Different Types of Shear Connectors

In steel-concrete composite structure, the shear force between structural steel and concrete is critical, which can be transferred via natural bonding, or shear connectors. Comparing with natural bonding, shear connectors is a more effective way to transfer the shear force [22, 23]. Stud and perfobond connectors are two most widely used shear connectors. Figure 27(a) shows the most commonly used stud with cylindrical head, which has excellent drawing capacity, welding quality, and shear force transferring ability [24~26]. Figure 27(b) shows the configuration of perfobond shear connector, which is the steel plate with holes arranged in the direction of shear force. Steel bars can be arranged penetrating

these holes to furtherly increase the shear strength of the connector [27, 28].
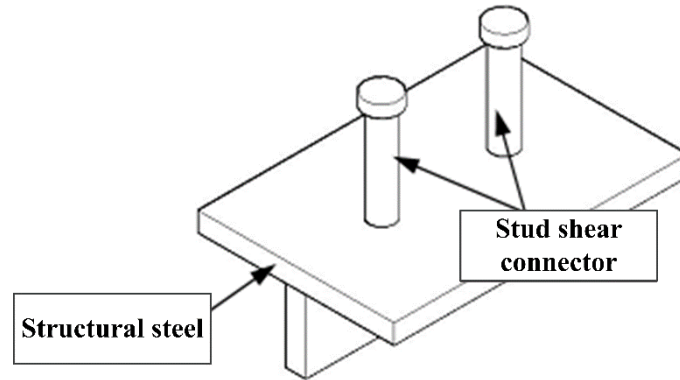
(a) Stud shear connector
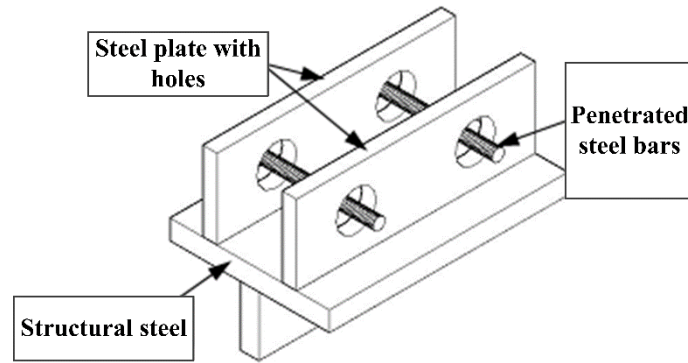
(b) Perfobond shear connector

Figure 26 Two types of shear connectors

Three types of concrete encased steel composite column were proposed in this study with different types of shear connectors, as shown in Figures 28(b)-(d). SCP-A in Figure 27(a), as introduced in Section 2.3, is the base specimen for comparison. SCP-G1 arranges stud shear connectors in steel-plate hooping; SCP-G2 uses perforate steel plate, namely, the perfobond shear connector without penetrated steel bars; SCP-G3 is designed based on SCP-G2, in which penetrated steel bars are placed aiming to achieve higher shear strength. The specimen SCP-G1~G3 have the same size of equal-leg angle, steel-plate hooping ratio, and shear-span ratio as the base specimen SCP-A. However, varying axial compression ratios were applied for SCP-G1~G3 to study how the ratio affects stress distribution of structural

steel and shear connectors.

Similar finite element modelling techniques were used for specimens SCP-G1~G3 as introduced before except the finite element type for structural steel. For specimen introduced in Section 2.1, shell element was used to simulate the equal-leg angle and steel-plate hooping. While for specimens G1~G3, solid element with refined mesh was used for modelling the stud, steel-plate hooping, and penetrated steel bars. Here solid element was also adopted for equal-leg, aiming to be consistent with the modeling of shear connectors and provide more accurate modelling results.

(a) SCP-A   (b) SCP-G1   (c) SCP-G2   (d) SCP-G3
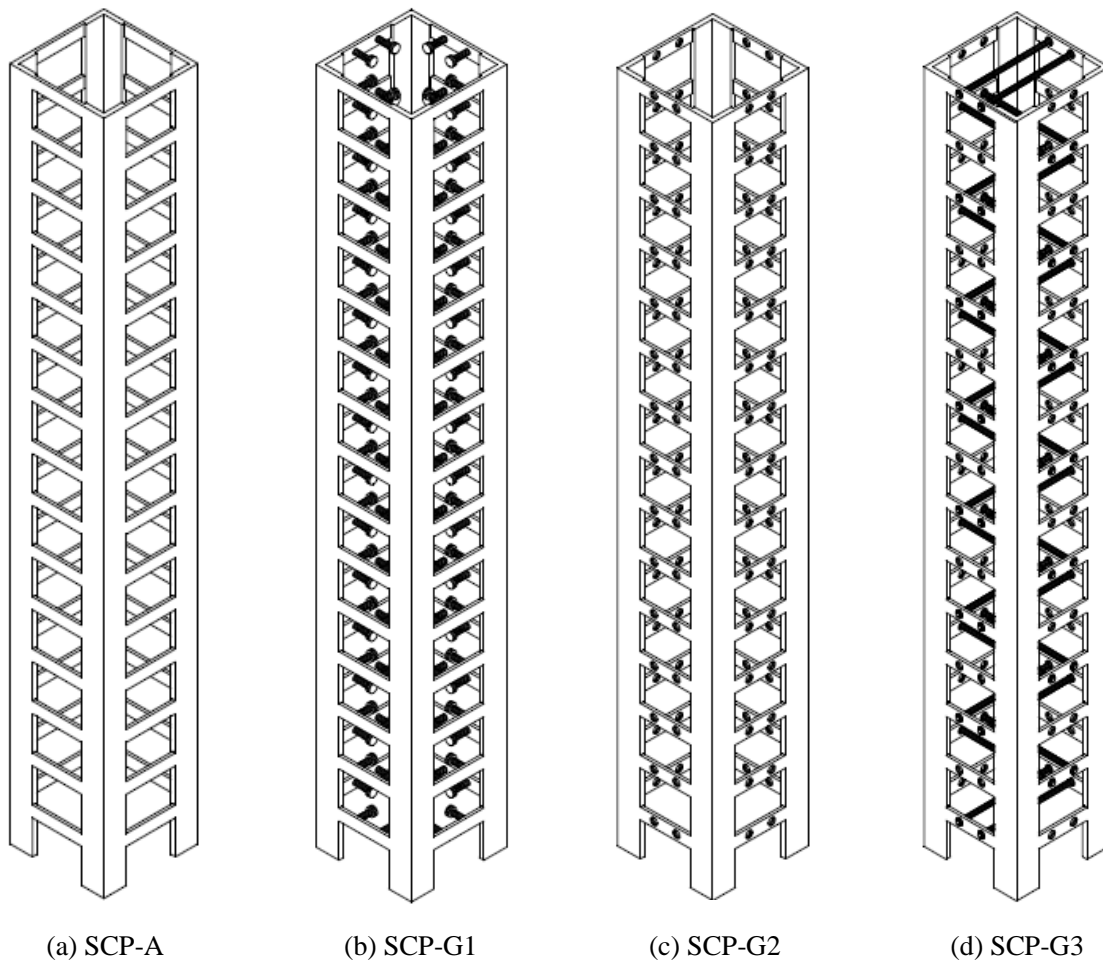
Figure 27 Configuration of specimen SCP-A and composite columns with different shear connectors

4.2 Lateral Load-Displacement Relation

Figure 28 shows lateral load-displacement curves for specimens SCP-A and SCP-G1~G3 under the axial compression ratio of 0.1. These four curves are generally consistent, showing

that arranging shear connectors did not affect the stiffness and strength of the composite columns under the axial compression ratio of 0.1. SCP-A has the largest maximum lateral displacement, which was followed by SCP-G1. SCP-G2 and SCP-G3 have similar maximum lateral displacement, which are smaller than that of SCP-A and SCP-G1. The difference of ultimate lateral displacement shows arranging shear connectors would decrease the displacement ductility of specimens in this study. Under small axial compression ratio, arrangement of shear connectors somewhat affects the integrity of concrete, and stress concentration is prone to occur between structural steel and concrete, reducing of the maximum lateral displacement. Thus, shear connectors are not recommended under small axial compression ratio.
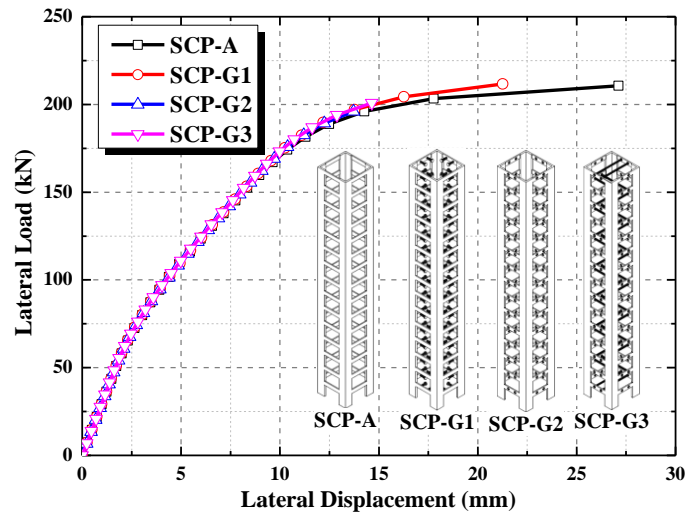
Figure 28 Lateral load-displacement curves of SCP-A and SCP-G1~G3

4.3 Stress of Structural Steel

Von mises stress of structural steel is studied under the axial compression ratio of 0.1, and stresses at centerline of the steel angle on the tension and compression sides from column top down to column bottom are extracted for analysis, as shown in Figure 29.

Figures 30–32 show von Mises stress on the compression and tension sides of SCP-G1~G3 under different axial compression ratio. It is necessary to mention that, vertical distance is set as x axis, and y axis shows the von Mises stress at different height. As the axial compression ratio increases, yield length of structural steel at compression side increases

significantly, as shown in Figures 30(a), 31(a), and 32(a). From the column top down to the bottom, stress of structural steel at tension side firstly decreases, and then gradually increase to yield stress, as shown in Figures 30(b),31(b), and 32(b). The structural steel in the composite column is under two forces which are balanced to a certain extent: axial compression, and tension due to the bending moment created by the horizontal loading. Near the column top as the moment arm is quite small, the tension resulting from the horizontal loading is smaller than the pre-compression. As the distance from the column top increases, the balance effect gradually increases, making the von Mises stresses reduces continually. Near the column bottom, the tension is the dominate force, and gradually increase to yield stress. No significant differences occur among these stress curves for SCP-G1~G3, indicating the type of shear connector seldom affect the stress of structural steel in this study.
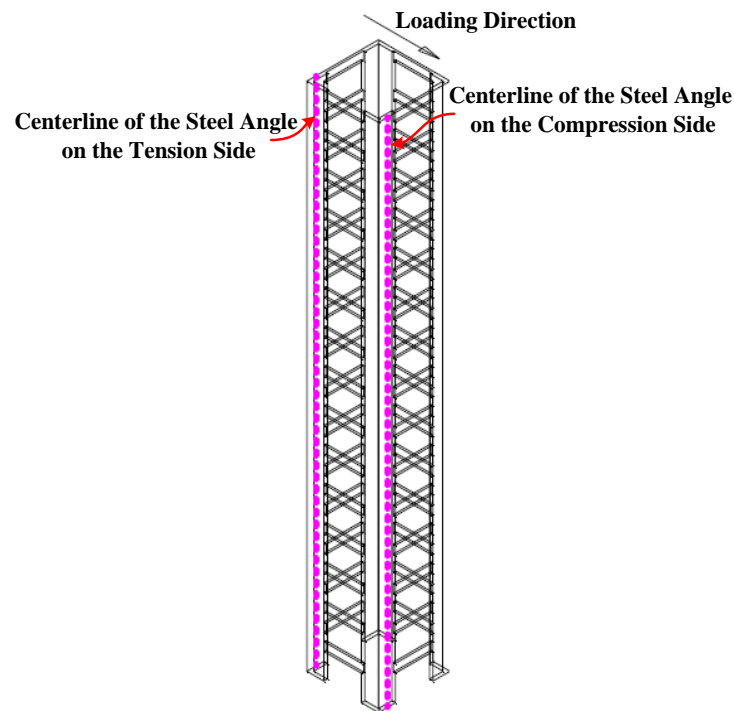
Figure 29 Stress extraction at centerline of the steel angle on tension and compression sides
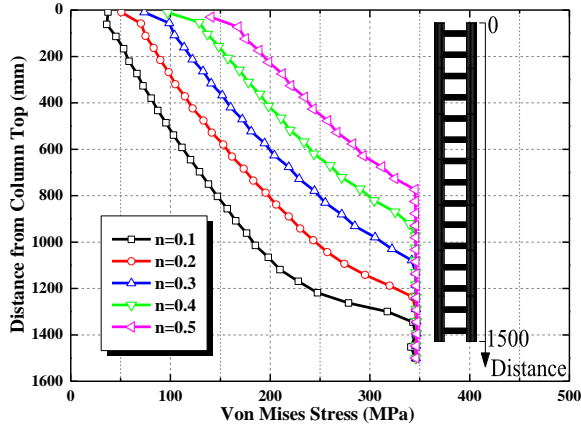
(a) Compression side
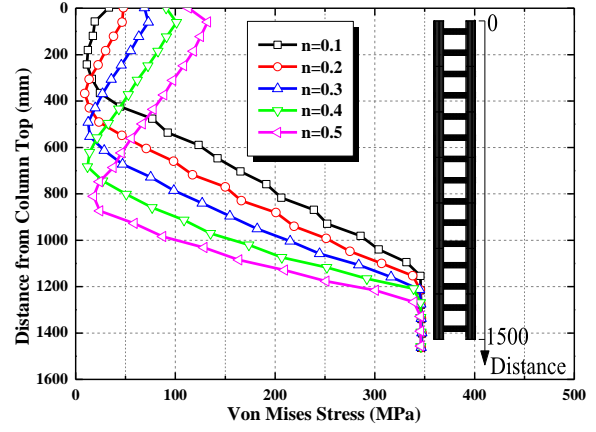
(b) Tension side

Figure 30 Von Mises stress of SCP-G1 under different axial compression ratio
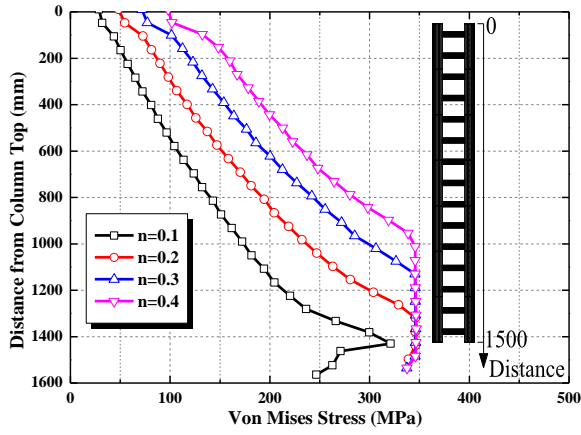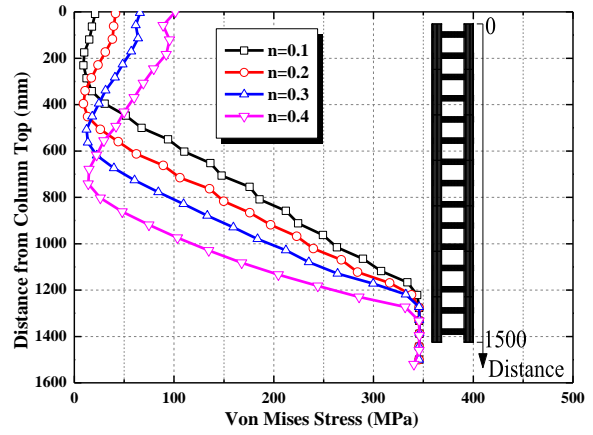
(a) Compression side

(b) Tension side

Figure 31 Von Mises stress of SCP-G2 under different axial compression ratio
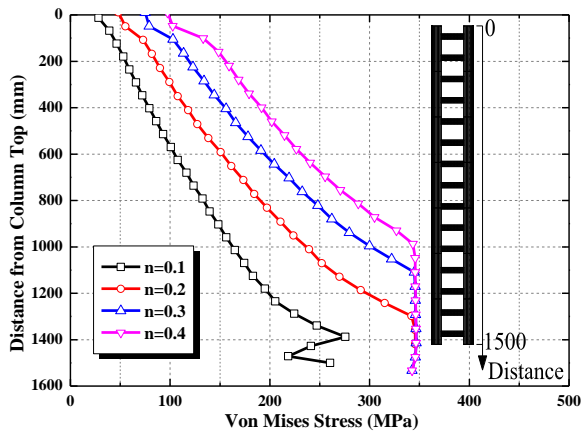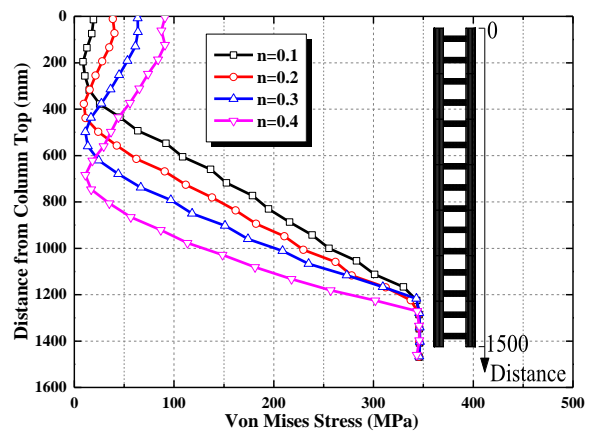
(a) Compression side

(b) Tension side

Figure 32 Von Mises stress of SCP-G3 under different axial compression ratio

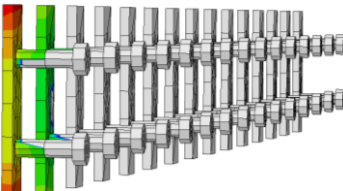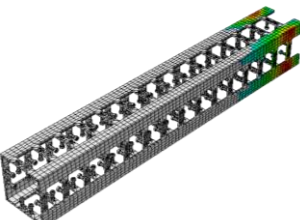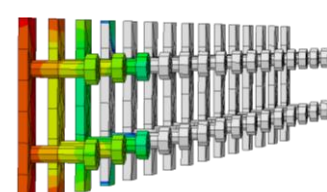## 4.4 Stress of Shear Connectors under Different Axial Compression Ratio
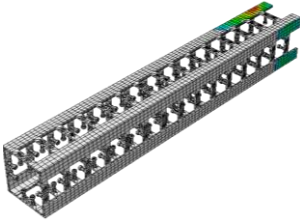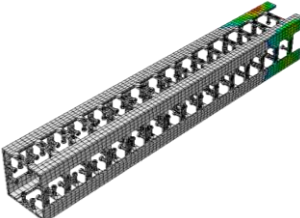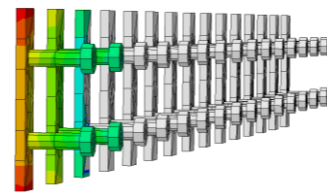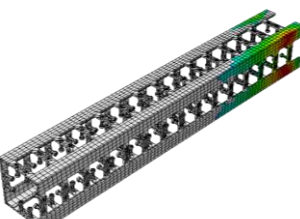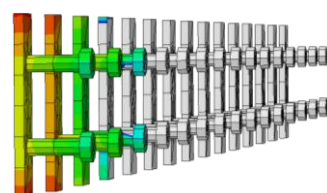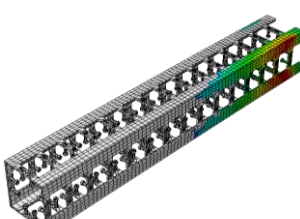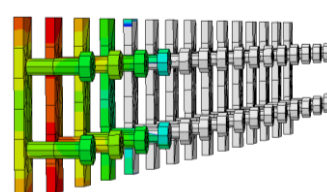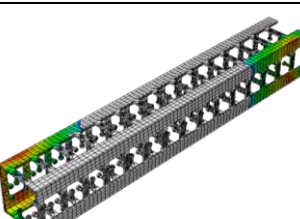
Shear connectors are critical to transfer and redistribute forces between steel and concrete. The stress distribution of shear connectors is studied for the composite columns under different axial compression ratio.

Table 6 shows the von Mises stresses of steel section and stud shear connectors for SCP-G1 on the compression side at the column bottom and tension side at the column top. Note in the stress cloud image, chromatic area represents the yielded steel, and achromatic area corresponds to the unyielded steel. Under the axial compression ratio of 0.1, no stud shear connectors yield at column bottom or top. As the axial compression ratio increases, the rows of yielded stud connectors on the compression side at column bottom increase from two rows under axial compression ratio of 0.2 to four rows under axial compression ratio of 0.7. On the tension side at column top, stud connectors did not yield until the axial compression ratio reaches to 0.7. Tables 7 and 8 show the von Mises stresses of steel section and perfobond shear connectors for SCP-G2 and G3 on the compression side at the column bottom and tension side at the column top. Similarly, as the axial compression ratio increases, rows of yielded perfobond shear connectors at both the column top and bottom increase.

By comparing the stress of shear connectors in SCP-G1~G3 under different axial compression ratio, we found that: (1) SCP-G2 and G3 are more likely to yield than SCP-G1 under the same axial compression ratio, indicating shear connection of SCP-G2 and G3 are greater than SCP-G1; (2) In SCP-G1, connectors provide large connection when the axial compression ratio is large than 0.2. Thus, to provide good bonding between concrete and structural steel, it is recommended to arrange stud shear connectors close to the column top and bottom when the axial compression ratio is larger than 0.2; (3) In SCP-G2 and G3, connectors provide large connection when the axial compression ratio is larger than 0.3. Thus, it is recommended to arrange perfobond shear connectors close to the column top and bottom when the axial compression ratio is larger than 0.3; (4) Considering that penetrating the steel bar has tiny effect on the mechanical behavior of the composite column, it is not

recommended to penetrate the steel bars to ensure a better casting effect.

Table 6 Stress cloud image of SCP-G1 under different axial compression ratio

Axial compression ratio	Von Mises stress of structural steel	Stud connectors on the compression side of column bottom	Stud connectors on the tension side of column top
0.1		No yielding	No yielding
0.2			No yielding
0.3			No yielding
0.4			No yielding
0.5			No yielding
0.6			No yielding

| 0.7 | | | |
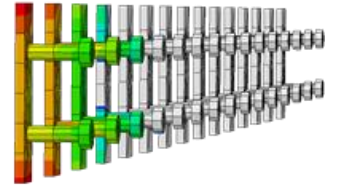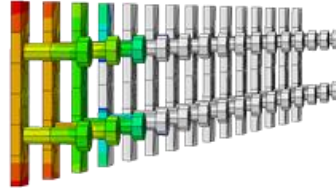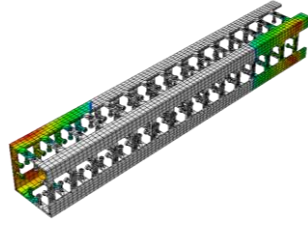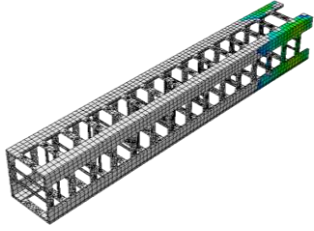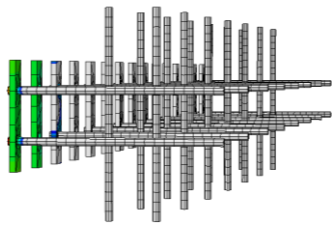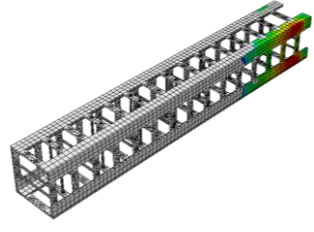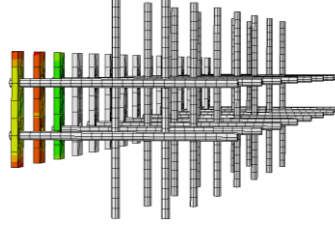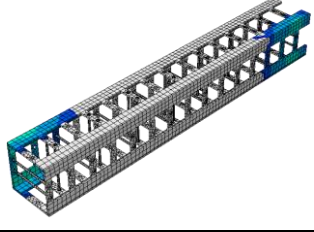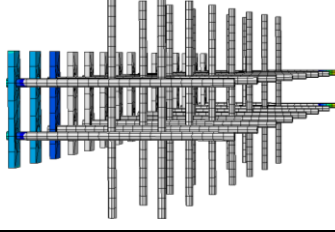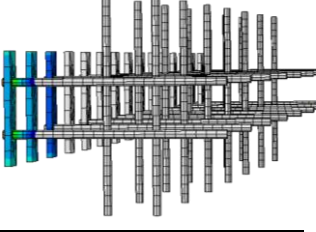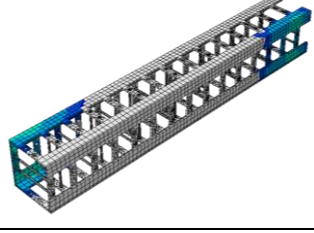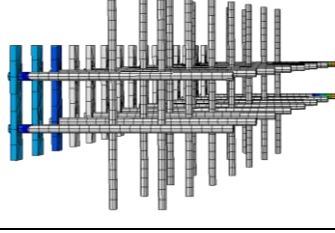
Table 7 Stress cloud image of SCP-G2 under different axial compression ratio

Axial compression ratio	Von Mises stress of structural steel	Perfobond connectors on the compression side of column bottom	Perfobond connectors on the tension side of column top
0.3			No yielding
0.4			No yielding
0.55			
0.65			
0.7			

Table 8 Stress cloud image of SCP-G3 under different axial compression ratio

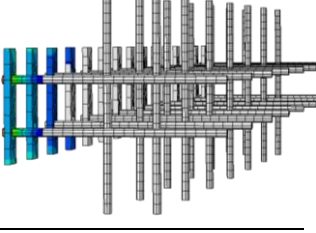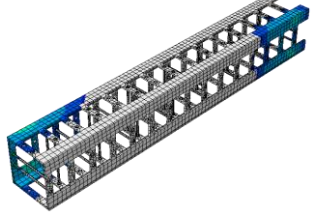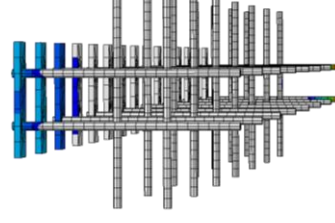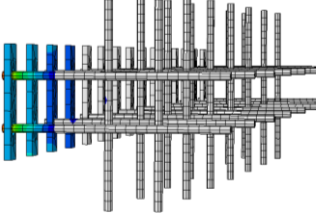| Axial compression ratio	Von Mises stress of structural steel	Perfobond connectors on the compression side of column bottom	Perfobond connectors on the tension side of column top
0.3			No yielding
0.4			No yielding
0.6			
0.7			
0.8			

35

5. Conclusion

Issues related to the ultimate load and ductility of concrete encased equal-leg angle steel composite columns were examined in this study. Parametric studies were performed to investigate the effects of different steel type, steel-plate hooping ratio, shear-span ratio, and axial compression ratio on the strength and ductility of the composite columns. In addition, composite columns with different types of shear connectors were proposed and the stress of angle steel and shear connectors under different axial compression ratio were investigated. The following conclusions can be made:

(1) Parameters include type of structural steel, steel-plate hooping ratio, shear-span ratio, and axial compression ratio were investigated on how they affect the strength and ductility of the composite columns. Equal-leg angle steel section encased in concrete column has larger strength and ductility than column with H-shaped steel. Increasing steel-plate hooping ratio result in greater displacement ductility of the composite columns, and increasing shear-span ratio give rise to decreasing displacement ductility. As axial compression ratio increases, displacement ductility almost linearly decreases for specimens in this study.

(2) Different types of failure modes occur with different axial compression ratio. Compression ratio of 0.35 corresponds to the balance failure mode in this study. The strain cross-section at column bottom linearly distributed under the axial compression ratio of 0.1, whereas the strain distribution is nonlinear when the axial compression ratio increases to 0.2, 0.4 and 0.5.

(3) The shear strength provided by perfobond connectors are larger than that provided by stud shear connectors for specimens under the same axial compression ratio. It is not recommended to arrange shear connectors for the columns with quite small axial compression ratio like 0.1, while it is recommended to arrange stud shear connectors near the column top and bottom as the axial compression ratio is larger than 0.2 and arrange perfobond shear connectors as the axial compression ratio is larger than 0.3. Considering that penetrating the steel bar has tiny effect on the mechanical behavior of the composite column, it is not recommended to penetrate the steel bars to ensure a better casting effect.

6.Acknowledgments

7. References

[1] "Hybrid Hollow High pier". 2018. 20 January 20, 2019. http://www.actec.or.jp/3h_pier/pdf/3h_pier_pamphlet.pdf

[2] Michio, O., et al. "Development of new high bridge piers containing spiral reinforcement." *Wind and Seismic Effects. Proceedings of the 30th Joint Meeting*. 1998.

[3] Diwei Zhang, et al. "Design and Construction of Sun Yat-Sen Freeway Widening Works from Wugu to Yangmei." *Transportation Standardization* 42.17 (2014): 61-71. (in Chinese)

[4] El-Tawil, Sherif, and Gregory G. Deierlein. "Strength and ductility of concrete encased composite columns." *Journal of Structural engineering* 125.9 (1999): 1009-1019.

[5] Soliman, K. Z., A. I. Arafa, and Tamer M. Elrakib. "Review of design codes of concrete encased steel short columns under axial compression." *HBRC journal* 9.2 (2013): 134-143.

[6] Ellobody, Ehab, and Ben Young. "Numerical simulation of concrete encased steel composite columns." *Journal of Constructional Steel Research* 67.2 (2011): 211-222.

[7] Chen, Cheng-Chih, and Nan-Jiao Lin. "Analytical model for predicting axial capacity and behavior of concrete encased steel composite stub columns." *Journal of Constructional Steel

Research 62.5 (2006): 424-433.

[8] Junji Shi., et al. "Structural performance of concrete encased steel columns with H-shaped steel." *Proceedings of 15th World Conference on Earthquake Engineering. Lisbon.* 2012.

[9] Junhua Li. *Study on the Performance of Steel Reinforced High-Strength Concrete Columns under Low Cyclic Reversed Lo*ading. Diss. Xi'an University of Architecture and Technology, 2005. (in Chinese)

[10] Zheng, Wenzhong, and Jing Ji. "Dynamic performance of angle-steel concrete columns under low cyclic loading-II: parametric study." *Earthquake Engineering and Engineering Vibration* 7.2 (2008): 137. American Institute of Steel Construction. *Specification for Structural Steel Buildings.* American Institute of Steel Construction, 2016.

[12] Ministry of Housing and Urban-Rural Development of the People's Republic of China (MOHURD). *Code for Design of Composite Structures, JGJ 138-2016.* China Architecture & Building Press, 2016. (In Chinese)

[13] Jing, Shi, and Bai Guo-liang. "AN EXPERIMENTAL STUDY ON RESTORING FORCE CHARACTERISTICS OF LATTICE TYPE STEEL REINFORCED CONCRETE FRAME COLUMNS." *JOURNAL OF XI'AN HIGHWAY UNVERSITY* 20.4 (2000).

[14] Zeng, L., et al. "Cyclic performance of concrete-encased composite columns with T-shaped steel sections." *International Journal of Civil Engineering* 13.4 (2015): 455-467.

[15] Ma, Hui, et al. "Seismic performance of steel-reinforced recycled concrete columns under low cyclic loads." *Construction and Building Materials* 48 (2013): 229-237.

[16] Zheng, Wenzhong, and Jing Ji. "Dynamic performance of angle-steel concrete columns under low cyclic loading-I: Experimental study." *Earthquake Engineering and Engineering*

Vibration 7.1 (2008): 67-75.

[17] Standard, Chinese. " Code for design of composite structures (JGJ 138–2016)." *The Chinese construction industry edition club, Beijing, China* (2016). (In Chinese)

[18] Mander, John B., Michael JN Priestley, and R. Park. "Theoretical stress-strain model for confined concrete." *Journal of structural engineering* 114.8 (1988): 1804-1826.

[19] Loh, H. Y., Brian Uy, and M. A. Bradford. "The effects of partial shear connection in the hogging moment regions of composite beams Part II—Analytical study." *Journal of Constructional Steel Research* 60.6 (2004): 921-962.

[20] Abaqus, Ver. "6.14 Documentation." Dassault Systemes Simulia Corporation 651 (2014).

[21] Park, R. "Evaluation of ductility of structures and structural assemblages from laboratory testing." *Bulletin of the New Zealand national society for earthquake engineering* 22.3 (1989): 155-166.

[22] Lam, Dennis, and Ehab El-Lobody. "Behavior of headed stud shear connectors in composite beam." *Journal of Structural Engineering* 131.1 (2005): 96-107.

[23] Xue, Dongyan, et al. "Static behavior of multi-stud shear connectors for steel-concrete composite bridge." *Journal of Constructional Steel Research* 74 (2012): 1-7.

[24] Lin, Zhaofei, Yuqing Liu, and Jun He. "Behavior of stud connectors under combined shear and tension loads." *Engineering Structures* 81 (2014): 362-376.

[25] WANG, Qian, and Yuqing LIU. "Experimental study of shear capacity of stud connector." *Journal of Tongji University (Natural Science)* 5 (2013): 004.

[26] Wang, Qian, et al. "Experimental study on stud shear connectors with large diameter and high strength." *Electric Technology and Civil Engineering (ICETCE), 2011 International Conference on*. IEEE, 2011.

[27] ZHAO, Chen, and Yu-qing LIU. "EXPERIMENTAL STUDY OF SHEAR CAPACITY OF PERFOBOND CONNECTOR [J]." *Engineering Mechanics* 12 (2012): 051.

[28] Zheng, Shuangjie, et al. "Shear behavior and analytical model of perfobond connectors." *Steel and Composite Structures* 20.1 (2016): 71-89.